AIAA JOURNAL
Vol. 40, No. 4, April 2002

# Accurate Numerical Simulation of Compressible Transitional Flows in Turbomachinery

P. De Palma*
*Politecnico di Bari, 70125 Bari, Italy*

**An accurate and efficient methodology is provided for computing turbulent and transitional flows by solving the compressible Reynolds-averaged Navier–Stokes equations with an explicit algebraic stress model and $k$–$\omega$ turbulence closure. The space discretization is based on a finite volume method with Roe's approximate Riemann solver and formally second-order-accurate MUSCL extrapolation. Second-order accuracy in time is achieved using a dual time-stepping technique combined with an explicit Runge–Kutta scheme and multigrid acceleration to converge the false transient at each physical time level. The turbulence model has been validated computing the vortex shedding behind a two-dimensional turbine cascade. Furthermore, the transition model of Mayle for separated flow has been combined with such a turbulence model; this methodology has been validated computing the flow through the T106 low-pressure turbine cascade with separated-flow transition at the suction-side boundary layer. Finally, the three-dimensional flow through the T106 linear cascade has been computed providing the analysis of the loss-coefficient distribution downstream of the cascade and the description of the interaction between the secondary flow pattern and the suction-side separation bubble.**

## Introduction

THE fundamental role of laminar–turbulent transition in gas-turbine engines has been widely recognized, for example, see the review by Mayle.[1] Although the main flow, in such engines, is highly turbulent, the flow regions close to the solid surfaces may be either laminar or turbulent. In turbomachinery flows, the transition may occur mainly in three ways. For high freestream turbulence levels, which are typical of gas-turbine engines, the development and amplification of Tollmien–Schlichting waves, which characterizes the natural transition process, is bypassed and turbulent spots are directly produced within the boundary layer due to the freestream disturbances. This first transition mode is known as bypass transition. The second transition mode may occur when a laminar boundary layer separates. In this case, transition occurs in the free-shear-layer-like flow close to the surface and a laminar-separation/turbulent-reattachment bubble is created at the wall.[1] Such a transition mode, known as separated-flow transition, may occur in adverse pressure-gradient regions, which can be found in both compressor and turbine cascades. Finally, transition in gas-turbine engines may be induced by the periodic passing of wakes (also trailing shock waves if the engine operates at transonic regime) from upstream blades and is called wake-induced transition.

In particular, the present paper deals with separated-flow transition. To obtain a reasonable prediction of losses and heat transfer for gas-turbine engines, numerical methods must be able to model the development of boundary layers through transition. Using the low Reynolds number $k$–$\omega$ model,[2] the author has developed a methodology for the solution of the Reynolds-averaged Navier–Stokes equations,[3] which then has been improved[4] by using the explicit algebraic stress model (EASM) of Ref. 5. In the present work, this methodology has been supplied with the model for separated-flow transition proposed by Mayle.[1] First, the EASM has been validated vs unsteady flows computing the vortex shedding behind the two-dimensional turbine cascade of Ref. 6. Then, the two-dimensional flow through the T106 turbine cascade[7] has been computed, with and without transition. Such a test case is suitable for validating the proposed methodology due to the separated-flow transition, which occurs at the rear part of the suction side of the blade. Finally, the three-dimensional flow through the T106 linear cascade has been computed comparing the results obtained employing the standard $k$–$\omega$ turbulence model and the EASM, with and without transition. In particular, the loss-coefficient distribution downstream of the cascade has been studied to demonstrate the effectiveness of the proposed approach.

In the following, the governing equations are given together with the details of the turbulence and transition models. Then, the numerical methodology is briefly described. Finally, the results concerning fully turbulent and transitional-flow computations are discussed.

## Governing Equations

The Reynolds-averaged Navier–Stokes equations, closed by the $k$–$\omega$ turbulence model,[2] are given by

$$\frac{\partial U}{\partial t} + \frac{\partial \left(F_i^c - F_i^v\right)}{\partial x_i} = S \tag{1}$$

where $U$ is the vector of the conservative variables,

$$U = \begin{pmatrix} \rho \\ \rho u_j \\ \rho E \\ \rho k \\ \rho \omega \end{pmatrix} \tag{2}$$

$F_i^c$, $F_i^v$, and $S$ are the components of the convective and viscous fluxes and the vector of the source terms, respectively,

$$F_i^c = \begin{pmatrix} \rho u_i \\ p\delta_{ij} + \rho u_i u_j \\ \rho u_i H \\ \rho u_i k \\ \rho u_i \omega \end{pmatrix}, \qquad F_i^v = \begin{pmatrix} 0 \\ \hat{\tau}_{ij} \\ b_i \\ (\mu + \sigma^* \mu_t)\dfrac{\partial k}{\partial x_i} \\ (\mu + \sigma \mu_t)\dfrac{\partial \omega}{\partial x_i} \end{pmatrix}$$

Received 5 July 2001; revision received 13 November 2001; accepted for publication 19 November 2001. 

*Associate Professor, Dipartimento di Ingegneria Meccanica e Gestionale, Centro di Eccellenza in Meccanica Computazionale, Via Re David 200; depalma@poliba.it. Member AIAA.

$$S = \begin{pmatrix} 0 \\ 0 \\ 0 \\ \tau_{ij}\dfrac{\partial u_i}{\partial x_j} - \beta^*\rho\omega k \\ \dfrac{\alpha\omega}{k}\tau_{ij}\dfrac{\partial u_i}{\partial x_j} - \beta\rho\omega^2 \end{pmatrix} \tag{3}$$

In Eqs. (1–3), $u_i$ are the components of the velocity vector, $p$ and $\rho$ are the pressure and the density, $k$ is the turbulence kinetic energy, and $\omega$ is the turbulence specific dissipation rate. Furthermore, $E = e + k + u_i u_i/2$ and $H = h + k + u_i u_i/2$ are the specific total internal energy and the specific total enthalpy, respectively. Finally, $\mu$ is the dynamic viscosity coefficient and $\mu_t$ is the eddy viscosity coefficient. Also, $\hat{\tau}_{ij}$ is the tensor of the viscous and Reynolds stresses:

$$\hat{\tau}_{ij} = 2\mu\left[\frac{1}{2}\left(\frac{\partial u_i}{\partial x_j} + \frac{\partial u_j}{\partial x_i}\right) - \frac{1}{3}\frac{\partial u_k}{\partial x_k}\delta_{ij}\right] + \tau_{ij} \tag{4}$$

where $\tau_{ij}$ is the Reynolds stress tensor given as

$$\tau_{ij} = 2\mu_t\left[\frac{1}{2}\left(\frac{\partial u_i}{\partial x_j} + \frac{\partial u_j}{\partial x_i}\right) - \frac{1}{3}\frac{\partial u_k}{\partial x_k}\delta_{ij}\right] - \frac{2}{3}\rho k\delta_{ij} \tag{5}$$

Furthermore, the energy fluxes are given as

$$b_i = u_j\tau_{ij} + \left(\frac{\mu}{Pr} + \frac{\mu_t}{Pr_t}\right)\frac{\partial h}{\partial x_i} + \left(\mu + \sigma^*\mu_t\right)\frac{\partial k}{\partial x_i} \tag{6}$$

where $Pr$ and $Pr_t$ are the laminar and turbulent Prandtl numbers, respectively. With regard to the two viscosity coefficients, $\mu$ is evaluated using Sutherland's law, whereas $\mu_t = \alpha^*\rho k/\omega$. The six closure parameters $\alpha^*$, $\alpha$, $\beta^*$, $\beta$, $\sigma^*$, and $\sigma$ are computed according to the low-Reynolds-number $k$–$\omega$ turbulence model[2]:

$$\alpha^* = \frac{\alpha_0^* + Re_t/R_k}{1 + Re_t/R_k}, \qquad \alpha = \frac{5}{9}\frac{\alpha_0 + Re_t/R_\omega}{1 + Re_t/R_\omega}\alpha^{*\,-1} \tag{7}$$

$$\beta^* = \frac{9}{100}\frac{\frac{5}{18} + (Re_t/R_\beta)^4}{1 + (Re_t/R_\beta)^4}, \qquad \beta = \frac{3}{40}, \qquad \sigma^* = \sigma = \frac{1}{2} \tag{8}$$

$$\alpha_0^* = \frac{\beta}{3}, \qquad \alpha_0 = \frac{1}{10}, \qquad R_\beta = 8, \qquad R_k = 6, \qquad R_\omega = 2.7 \tag{9}$$

where $Re_t$ is the turbulent Reynolds number, $Re_t = \rho k/\omega\mu$. Finally, the equation of state for perfect gases has been employed to complete the governing equations.

Standard characteristic boundary conditions are imposed at inflow and outflow boundaries. For the case of subsonic flow, which is considered in the present work, total enthalpy, total pressure, flow angle, turbulence kinetic energy, and turbulence specific dissipation rate are imposed at the inlet, whereas pressure is prescribed at the outlet. Furthermore, at the solid wall, the no-slip wall boundary condition is used, and the turbulence kinetic energy is set to zero. The pressure and the temperature at the wall are computed by forcing zero normal gradients. For the value of $\omega$ at the wall, the following condition has been employed (see Ref. 8): $\omega_w = 60\nu/\beta(\Delta y_w)^2$, where $\nu$ is the kinematic viscosity coefficient and $\Delta y_w$ is the distance between the wall and the first grid point away from the wall. In the present work, nonperiodic C grids are employed, namely, the two edges of the branch cut have a different number of cells. This feature enables the reduction of the distortion of the mesh in the blade channel. A conservative treatment of the boundary conditions at the branch cut is applied by using two rows of phantom cells, overlapping to the grid, in which the dependent variables are evaluated by linear interpolation.

## Explicit Algebraic Stress Model

The explicit nonlinear constitutive equation, obtained by Gatski and Speziale,[5] has been considered for the Reynolds stress tensor:

$$\tau_{ij} = 2\mu_t\left[S_{ij} - \tfrac{1}{3}S_{kk}\delta_{ij} + (\alpha_4/\omega)(S_{ik}W_{kj} + S_{jk}W_{ki}) + (\alpha_5/\omega)(S_{ik}S_{kj} - \tfrac{1}{3}S_{kl}S_{kl})\right] - \tfrac{2}{3}\rho k\delta_{ij} \tag{10}$$

where $S_{ij}$ and $W_{ij}$ are the mean rate of strain tensor and the mean vorticity tensor, respectively. In Eq. (10),

$$\mu_t = \frac{\rho\alpha^* C_\mu k}{C_\mu^0\omega} \tag{11}$$

where

$$C_\mu = \frac{3(1+\eta^2)\alpha_1}{3 + \eta^2 + 6\eta^2\xi^2 + 6\xi^2}, \qquad C_\mu^0 = 0.09$$

$$\eta^2 = \frac{\alpha_2}{\omega^2}(S_{ij}S_{ij}), \qquad \xi^2 = \frac{\alpha_3}{\omega^2}(W_{ij}W_{ij})$$

The closure coefficients, $\alpha_1$–$\alpha_5$, are evaluated as follows:

$$\alpha_1 = \left(\tfrac{4}{3} - C_2\right)(g/2), \qquad \alpha_2 = (2 - C_3)^2(g^2/4)$$

$$\alpha_3 = (2 - C_4)^2(g^2/4), \qquad \alpha_4 = (2 - C_4)(g/2)$$

$$\alpha_5 = (2 - C_3)g, \qquad g = 1/(0.5C_1 + C_5 - 1)$$

with $C_1 = 3$, $C_2 = 0.8$, $C_3 = 1.75$, $C_4 = 1.31$, and $C_5 = 2$. Such values correspond to the pressure–strain correlation model of Launder et al.,[9] already employed by Gatski et al.[10] in conjunction with the EASM of Ref. 5.

## Transition Model

The present paper focuses on separated-flow transition, understanding of which can be crucial for improving the performance of compressors and turbines (especially low-pressure) at off-design conditions. The base mechanism of the separated-flow transition has been described in detail in Ref. 1. The essential features are shown in Fig. 1, which provides a time-averaged representation of the transition region. After flow separation, there is a low-pressure-gradient region (upstream region) followed by a pressure recovery (downstream region). The upstream region is composed of a laminar shear flow, between the abscissas $x_s$ (separation) and $x_t$ (transition onset), and a transition region, between the abscissas $x_t$ and $x_T$ (end of transition). At the downstream region, the flow is turbulent and reattaches at $x_r$. When different sets of experimental data were considered, Mayle[1] proposed the following correlation:

$$(Re_x)_{st} = 1000Re_{\theta s}^{0.7} \tag{12}$$

where the Reynolds numbers are defined as

$$(Re_x)_{st} = U_s(x_t - x_s)/\nu_s, \qquad Re_{\theta s} = U_s\theta_s/\nu_s \tag{13}$$

where $U_s$, $\theta_s$, and $\nu_s$ are the freestream velocity, the momentum thickness, and the kinematic viscosity at the separation point. When Eq. (12) is used, it is possible to evaluate the distance between

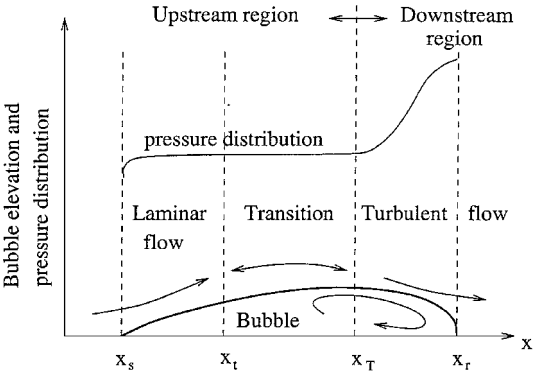


**Fig. 1 Flow around a separation bubble (from Ref. 1).**

the transition and the separation point, $x_t - x_s$, provided that the conditions at the separation point are known. Furthermore, Mayle provides a second experimental correlation,

$$(Re_x)_{\mathrm{LT}} = U_s(x_T - x_t)/\nu_s = 400Re_{\theta s}^{0.7} \tag{14}$$

which enables to estimate the length of the transition region, $x_T - x_t$. In such a region, the intermittency factor $I$ is evaluated as

$$I = 1 - \exp\left[-0.412\,\frac{(x - x_t)^2}{(x_{75} - x_{25})^2}\right] \tag{15}$$

where $x_{25}$ and $x_{75}$ correspond to the locations where $I$ is equal to 0.25 and 0.75, respectively, and $I = 0.99$ corresponds to the abscissa $x_T$ (Ref. 1). When such a value is inserted in Eq. (15) with knowledge of $(x_T - x_t)$ from Eq. (14), the difference $(x_{75} - x_{25})$ is evaluated. Therefore, for transitional-flow computations, the eddy viscosity is defined as $\mu_{\mathrm{tran}} = I\mu_t$. Equation (15) is an experimental correlation due to Dhawan and Narasimha,[11] which describes the growth of turbulence near walls. In the present work, no attempt has been made to improve the model recalibrating the preceding correlation for each turbulence model employed. Finally, for the iteration procedure employed in the present work, the computations start with the intermittency factor equal to zero everywhere. At the beginning, the flow separates from the blade surface near the trailing edge. When the flow characteristics at the separation point, that is, $U_s$, $\theta_s$ and $\nu_s$, are known, it is possible to compute $x_t$, using correlation (12) and the length of transition, $x_T - x_t$, from correlation (14). With iteration, the separation point shifts upstream along the suction side until it reaches a stable location; hence, the separation bubble, transition point, and transition length become stable.

## Space and Time Discretizations

A strongly coupled approach is employed for solving Eq. (1), that is, the Navier–Stokes equations and the turbulence model equations are solved as a unique set. A finite volume method is used, based on the flux difference splitting technique proposed by Roe[12] for the discretization of the convective terms. Initial data for the Riemann problem at each interface are computed using a formally second-order-accurate, fully upwind MUSCL extrapolation with minmod limiter. The diffusive contributions are discretized employing central differencing: At each interface the derivatives of the primitive variables are computed using Green's theorem and a dual cell centered at the interface, whereas the dependent variables are obtained averaging adjacent cell-center values. Finally, the derivatives employed to evaluate the source terms are obtained using Green's theorem over each cell.

For the present computations, an explicit (four-stage) Runge–Kutta time integration scheme is employed, with coefficients $\alpha_1 = \frac{1}{4}$, $\alpha_2 = \frac{1}{3}$, and $\alpha_3 = \frac{1}{2}$. Furthermore, to increase the efficiency, three well-known methods are used, namely, local time stepping, implicit residual smoothing (IRS), and multigrid strategy. The time step is evaluated as $\Delta t^* =$ Courant–Friedrichs–Lewy number (CFL) $(\Delta t^{*c}\Delta t^{*v})/(\Delta t^{*c} + \Delta t^{*v})$, where the convective, $\Delta t^{*c}$, and diffusive, $\Delta t^{*v}$, time steps are computed as provided in Ref. 13. At each stage of the Runge–Kutta scheme, the IRS with variable coefficient[14] is employed. In the present work, such a procedure allows the use of CFL = 3–4, depending on the test case. Finally, a standard full approximation storage (FAS) multigrid strategy[15] is employed to drive the residual of the governing equations to machine zero. A V-cycle has been used, with three or four grid levels, depending on the mesh size. Linear interpolations are employed to transfer the corrections from each coarse grid to the finer one.

For unsteady-flow computations, a dual time-stepping technique[16] is employed, the time derivative being discretized using a three-level backward formula. Between two physical time steps, the solution is advanced in the fictitious time by means of the preceding Runge–Kutta scheme with multigrid acceleration and IRS.

## Turbulent-Flow Computations

The unsteady turbulent flow through a large-scale nozzle guide vane has been considered for validating the EASM. The blade has a thick, rounded trailing edge, which causes the formation of a von Kármán vortex street due to the unsteady separation of the boundary layers. The main geometrical features of the cascade and the blade coordinates are provided in Ref. 6. Because of the relatively small aspect ratio, two fences were placed close to the endwall boundary layers to prevent the formation of secondary flows. In this way two-dimensional flow conditions exist over approximately 75% of the blade height, and for this reason, only two-dimensional flow computations are presented. The flow conditions are as follows: inlet total temperature $T_{t1} = 293$ K, inlet total pressure $p_{t1} = 1.178$ bar, isentropic exit Mach number $M_{2,\mathrm{is}} = 0.4$, turbulence intensity $Tu = 1.15\%$, Reynolds number, based on the axial chord and on outlet flow conditions, $Re = 2.8 \times 10^6$.

Unsteady computations, employing the EASM, have been performed using three C meshes with $256 \times 32$, $384 \times 48$, and $576 \times 72$ quadrilateral cells. The grids have 128, 192, and 288 cells on the profile, respectively. The corresponding average $y^+$ values at the first cell center close to the blade profile are 2.3, 1, and 0.5. Computations were performed using three time-step sizes, corresponding about to 40, 60, and 90 divisions of the shedding period, for the three grids, respectively. The $L^1$ norm of the residual of the continuity equation was reduced to $10^{-5}$ between two consecutive physical instants, requiring from 10 to 25 multigrid V-cycles depending on the grid employed.

A global view of the flow is provided in Fig. 2, where the instantaneous Mach number contours, computed using the fine grid, are shown.

The pressure time histories at two locations on the blade, $s/D = -1.7$ and 1.67, are provided in Fig. 3. The parameter $s$ is the curvilinear abscissa along the blade profile starting at the trailing edge (negative and positive values indicate the suction side and the pressure side, respectively), whereas $D$ is the trailing-edge diameter. After an initial time interval, a well-defined cyclic behavior is reached. The pressure fluctuations induced by the vortex shedding propagates far upstream in the boundary layers, as also found by experiments.[6,17]

For the experimental unsteady flow data provided in Refs. 6 and 17, the pressure signal at $s/D = 0.48$ has been recorded. The associated dominant frequency is 2.65 kHz, which corresponds to a Strouhal number (based on the trailing-edge diameter and on the isentropic exit velocity) equal to 0.297. The computed dominant

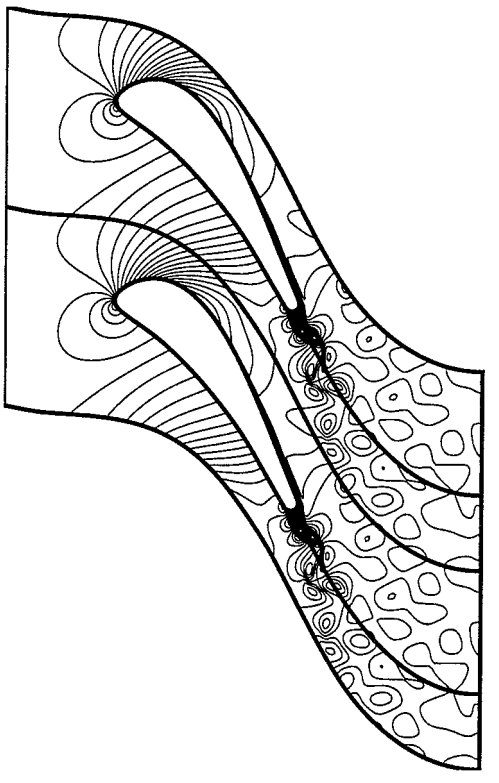

**Fig. 2 Mach number contours on the fine grid ($\Delta M = 0.02$).**

frequencies are 1.81, 2.15, and 2.32 kHz for the coarse, medium, and fine grid, respectively, which correspond to Strouhal numbers equal to 0.2, 0.238, and 0.258. Such values are close to the ones obtained employing the standard $k-\omega$ model[3] and are slightly lower than the experimental one; nevertheless, they fall in the typical range of blades with fully turbulent boundary layers on both sides of the trailing edge.

The isentropic Mach number distributions along the blade profile are shown in Fig. 4. The symbols refer to the experimental data of Ref. 6, whereas the lines refer to the computed results (time averaged over 50 cycles). The numerical results agree quite well with the experimental data. The lines corresponding to the medium and fine grid are coincident within plotting accuracy, demonstrating grid convergence. The curve corresponding to the coarse grid is very close to the earlier ones except at the trailing-edge region, where an unphysical sudden overcompression is predicted due to the poor grid resolution.

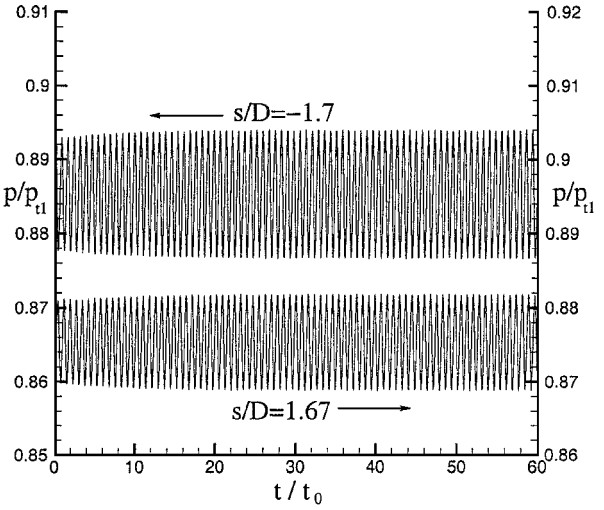


**Fig. 3 Pressure time histories.**

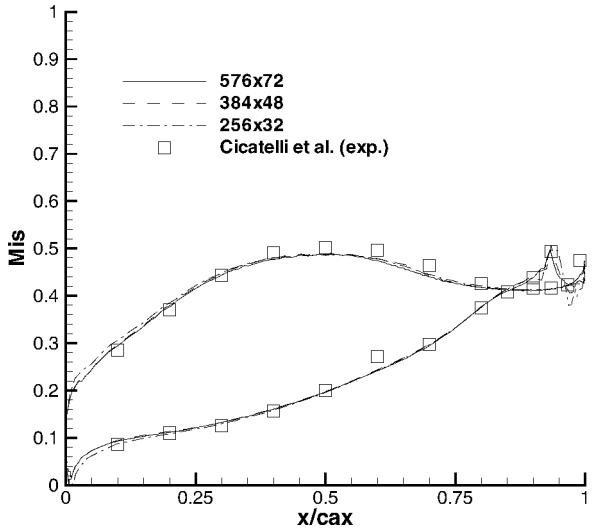


**Fig. 4 Isentropic Mach number distribution.**

Figure 5 shows the boundary-layer velocity distributions at two locations corresponding to $s/D = \pm 1.75$. The symbols refer to the experimental data, the squares and the circles indicate the suction side and the pressure side, respectively. The numerical results obtained using the standard $k-\omega$ model and the EASM have been reported in Fig. 5 for comparison. The lines, referring to the numerical results, show a convergence of the profiles toward the experimental distributions, which are very close to the fine grid results. A comparison between experimental and numerical data, obtained using the EASM, for the characteristics of the boundary layers at the same locations are given in Table 1. In particular, Table 1 gives the thickness $\delta$, the displacement thickness $\delta^*$, the momentum thickness $\theta$, and the shape factor $H$, where $\delta$, $\delta^*$, and $\theta$ are nondimensionalized with respect to the trailing-edge diameter $D$. The data clearly indicate that both boundary layers are turbulent. Furthermore, the numerical data, obtained using the fine grid, agree fairly well with the experimental data.

## Transitional-Flow Computations

The linear turbine cascade T106 has been considered as a suitable test case for two-dimensional and three-dimensional computations (see Ref. 18 for geometrical details). The flow is subsonic with isentropic exit Mach number equal to 0.59; Reynolds number equal to $5 \times 10^5$, based on the chord length $c$ and on exit conditions; inlet flow angle equal to 37.7 deg (with respect to the horizontal line); and inlet turbulence length scale equal to $0.02c$ (Refs. 7 and 18). Experiments indicate that a separated-flow transition occurs for freestream turbulence levels $Tu$ in the range $0.8\% \le Tu \le 7.1\%$ (Ref. 7). For the case with $Tu = 0.8\%$, two-dimensional turbulent unsteady-flow computations have been performed, employing the EASM without transition model. Three C grids have been considered with $256 \times 32$, $384 \times 48$, and $576 \times 72$ cells. The grids have 128, 192, and 288 cells along the profile, respectively, the corresponding average nondimensional distances of the first cell center

**Table 1 Boundary-layers characteristics**

| | Pressure side | | Suction side | |
|---|---|---|---|---|
| Characteristic | Experiment | $576 \times 72$ | Experiment | $576 \times 72$ |
| $\delta/D$ | 0.134 | 0.139 | 0.277 | 0.292 |
| $\delta^*/D$ | 0.0167 | 0.0160 | 0.0405 | 0.0389 |
| $\theta/D$ | 0.0102 | 0.0094 | 0.0288 | 0.0266 |
| $H$ | 1.64 | 1.70 | 1.41 | 1.46 |

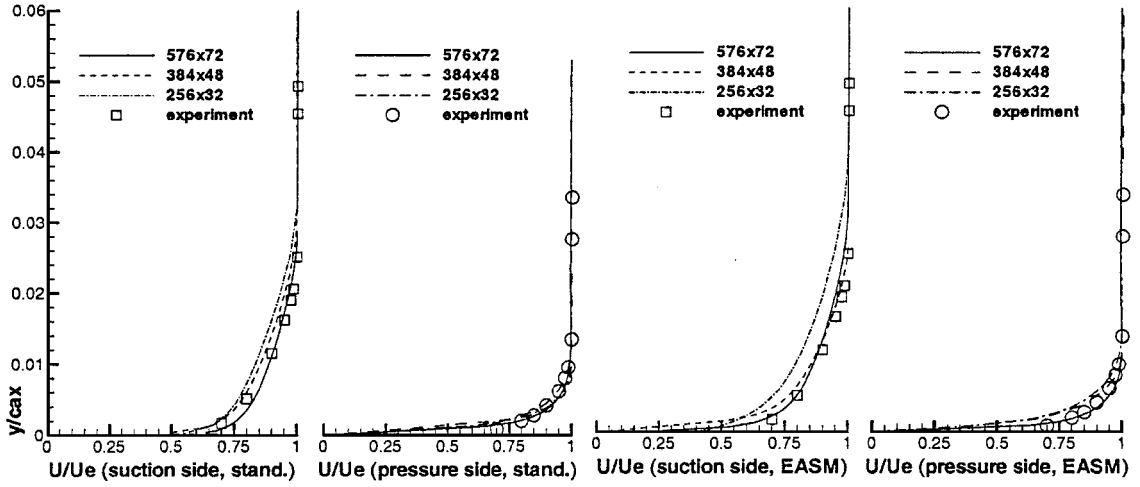


**Fig. 5 Boundary-layer velocity profiles at $S/D = -1.75$ (•) and $S/D = 1.75$ (□), for the standard $k-\omega$ model and the EASM.**

from the wall, $y^+$, being about 2, 1, and 0.5. The computations provide only small-pressure oscillations in time around the trailing edge, which do not affect the shape and position of the bubble. All results presented in the present section are averaged in time. Figure 6 provides the comparison between the computed and experimental[19] distributions of the pressure coefficient $C_p = (p - p_2)/(p_{t1} - p_2)$, where $p_{t1}$ and $p_2$ are the inlet total pressure and the exit static pressure, respectively. The four distributions are very close to each other except at the rear part of the suction side where the solution obtained using the coarse grid does not predict separation. This is also clearly shown in Fig. 7, where the comparison between numerical and experimental boundary-layer profiles at five locations along the suction side of the blade are provided. The medium-grid (dashed line) and the fine-grid (solid line) solutions are very close to each other and agree fairly well with the experimental data indicating the presence of the separation bubble. Examination of the skin-friction coefficient distribution (not shown) shows that a large part of the suction-side boundary layer is laminar, in agreement with the experimental data.[7] When the fine and medium grids are used, the (free) transition is located about at $x/c = 0.85$ and 0.84, respectively, whereas when the coarse grid is used, transition is shifted upstream at about $x/c = 0.65$. Note that, when using the standard $k$–$\omega$ turbulence model (without transition model), the separation was not obtained even on the medium and the fine grids, due to the higher extension of the turbulent boundary-layer region along the suction side of the blade. Moreover, when the EASM (without transition model) is used and the freestream turbulence level is slightly increased, the separation bubble disappears, in contrast with the experimental data.

To capture the separation bubble in the range $0.8\% < Tu \leq 7.1\%$, it was necessary to employ the transition model described earlier. Figure 8 provides the comparison between the experimental data and the numerical data obtained using the EASM with the transition model and the medium grid. The three solid lines represent the experimental data, namely, the abscissa along the chord, $x/c$, corresponding to the point on the suction side at which separation (bottom line), transition (center line), and reattachment (top line) occur, respectively, vs the freestream turbulence level. The symbols represent the present numerical data computed with four levels of $Tu$, namely, 0.8, 2.7, 5.1, and 7.1%, which correspond to the conditions of the experimental data provided in Ref. 7. The agreement between the two sets of data can be considered fairly good. Note that the predictions of the separation, transition, and reattachment points obtained using the standard $k$–$\omega$ are very close to the ones shown in Fig. 8 obtained with the EASM. Moreover, in Fig. 9, the distribution of the boundary-layer momentum thickness (nondimensionalized with respect to the chord) along the suction side is provided, this parameter being relevant for the prediction of the transition. The symbols refer to the experimental data with $Tu = 0.8\%$ (circles) and $Tu = 5.1\%$ (squares), whereas the lines represent the corresponding numerical results (solid line and dashed line, respectively). Also, in this case, the agreement is fairly good especially at the transition region.

Finally, the three-dimensional flow through the linear turbine cascade T106 has been considered to study the secondary flows and the losses. Steady-flow computations have been performed with inlet turbulence intensity equal to 5.8% to compare the results with the experimental data reported in Ref. 18. Moreover, the measured[18] total-pressure spanwise profile has been prescribed at inlet points.

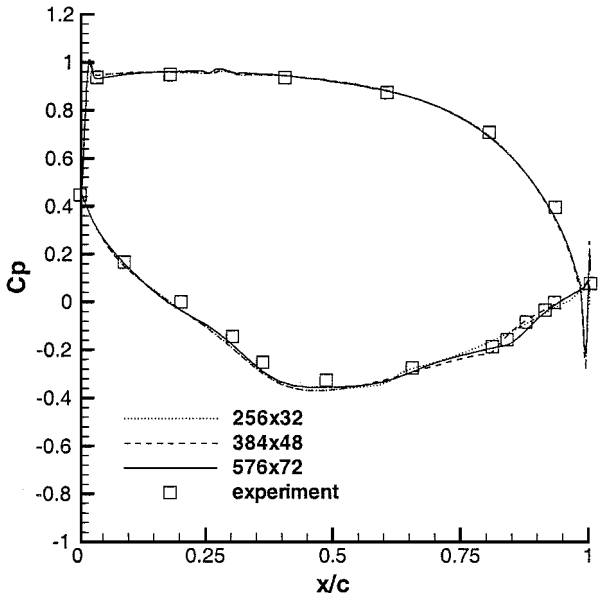


Fig. 6 Pressure-coefficient distribution.

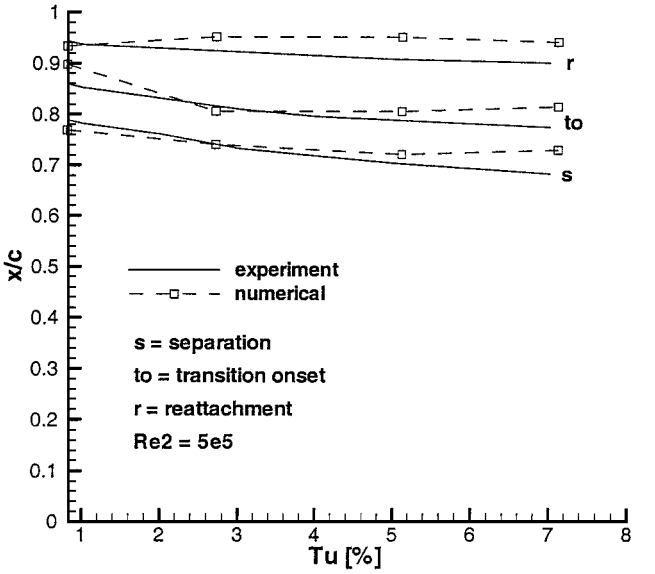


Fig. 8 Effect of the inlet turbulence intensity on separation, transition, and reattachment at the suction side.

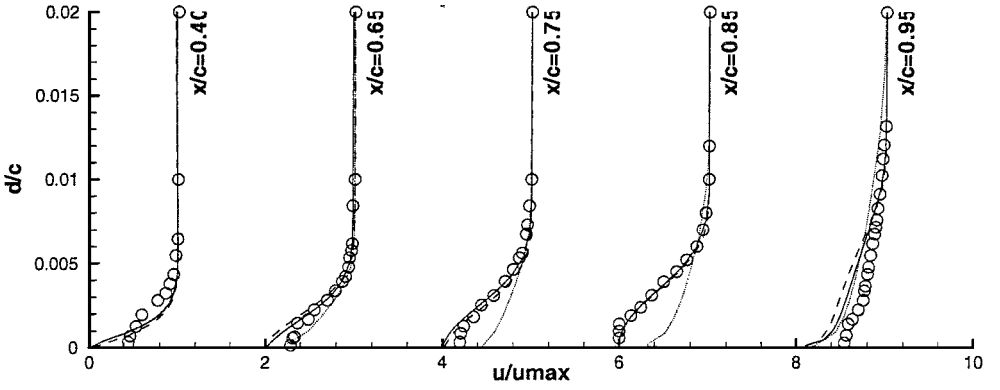


Fig. 7 Suction-side boundary-layer profiles.

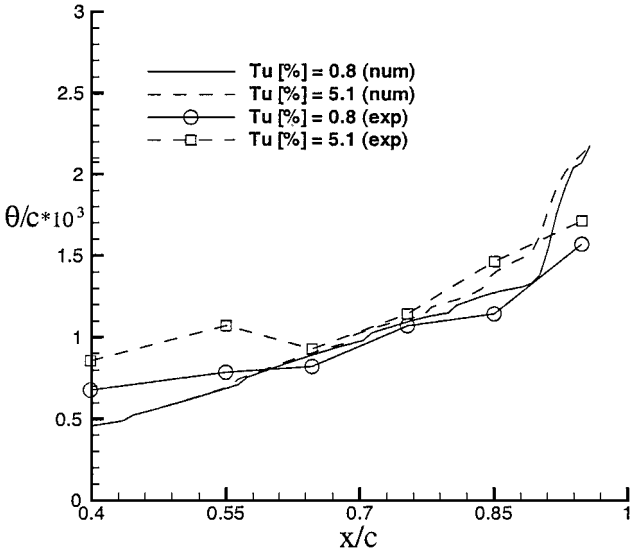


**Fig. 9 Boundary-layer momentum thickness along the suction side.**

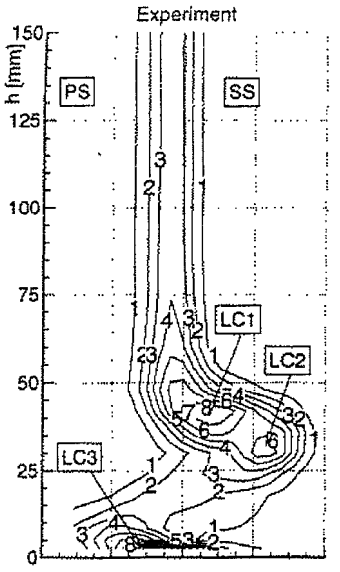


**Fig. 10 Loss-coefficient contours ($\Delta\zeta = 0.03$).**

A C grid has been employed with $384 \times 40 \times 48$ cells, which was proven adequate for the present calculation.[4] The average nondimensional distance of the first cell center from the blade surface is about $y^+ = 1$, whereas at the sidewall $y^+ = 2$. Four computations have been performed employing the standard turbulence model and the EASM, with and without transition. Figures 10–12 show the contours of the loss coefficient defined as $\zeta = (p_{t1} - p_t)/(p_{t1} - p_2)$, where $p_t$ is the total pressure and the subscripts 1 and 2 indicate inlet and outlet conditions, respectively. Figures 10–12 all refer to a plane located at $x/c_{ax} = 1.5$. Figure 10 provides the experimental data[18]: The distribution of the loss coefficient clearly shows a large two-dimensional flow region at midspan and is characterized by three loss cores (LCs). The principal one (LC1) originates between the the suction-side branch of the horseshoe vortex and the passage vortex; LC2 is directly related to the passage vortex, whereas LC3 is due to the counter-rotating corner vortex induced by the passage vortex in the corner between the sidewall and the suction side.[18] All of these features are well captured by the numerical solutions shown in Figs. 11 and 12. Note that all computations overestimate the losses. Nevertheless, employing the EASM, the local peak value of the loss coefficient in the wake is closer to the experimental data. Moreover, a further improvement in the prediction of the loss-coefficient distribution is achieved when the transition model is employed. In fact, the contours provided in Fig. 12b, which refer to the solution obtained with the EASM, are in good agreement with the experimental data of Fig. 10. Figure 13 provides the pitchwise-averaged

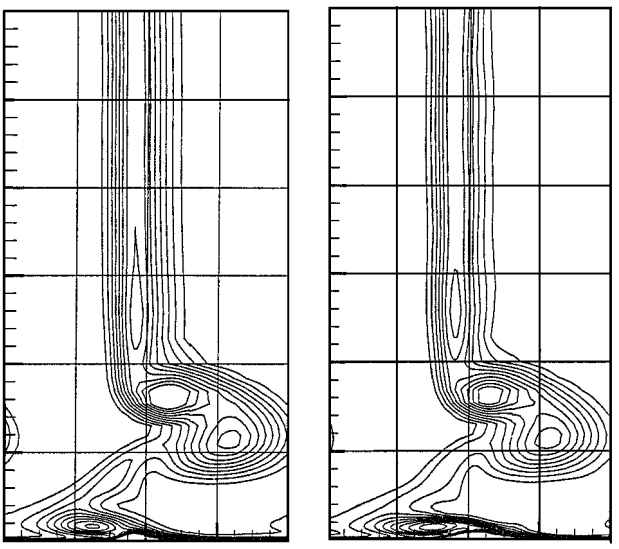


**Fig. 11 Loss-coefficient contours ($\Delta\zeta = 0.03$): turbulent-flow computations with a) standard model and b) EASM.**

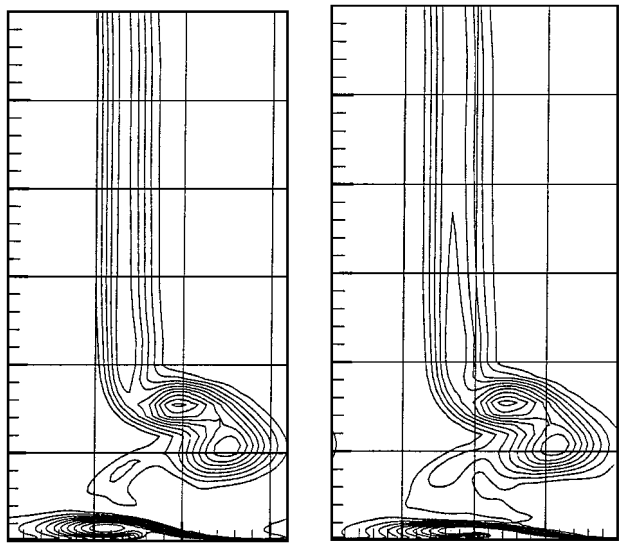


**Fig. 12 Loss-coefficient contours ($\Delta\zeta = 0.03$): transitional-flow computations with a) standard model and b) EASM.**

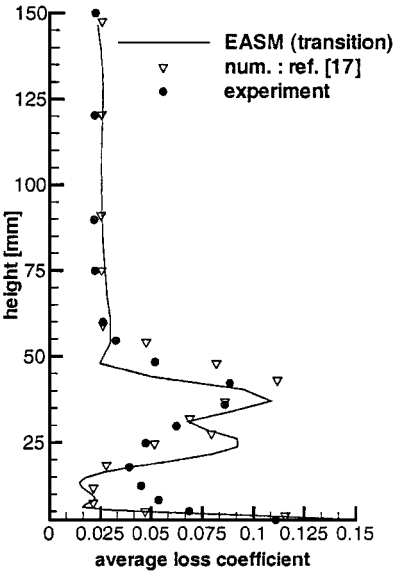


**Fig. 13 Average loss-coefficient distribution.**

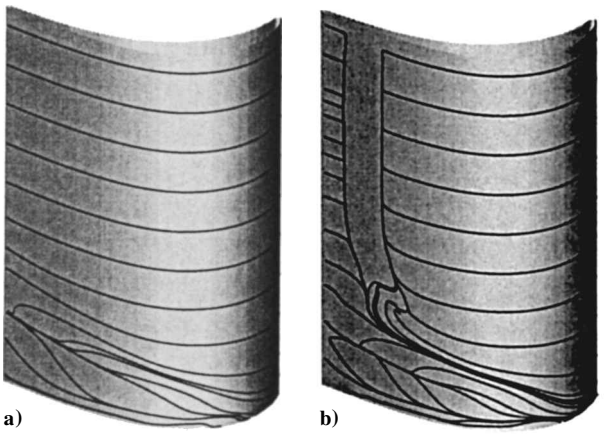


**Fig. 14 Stream traces at the suction surface: EASM a) without and b) with transition model.**

loss-coefficient distributions, defined as $\bar{\zeta} = (p_{t1} - \bar{p}_t)/(p_{t1} - p_2)$, where $\bar{p}_t$ is the mass-averaged total pressure, vs the blade height. The numerical results agree reasonably well with the experimental data and are very close to the numerical results of Ref. 18 (triangles), obtained using a finer multiblock grid (1,138,000 points) and a low-Reynolds-number $k$–$\epsilon$ turbulence model without transition model.

Finally, Fig. 14 provides two three-dimensional views of the stream traces close to the suction-side surface of the blade, computed employing the EASM without and with transition, respectively. The main difference between the two solutions is the separation bubble, which is clearly detected when employing the transition model. Both solutions show the evolution of the passage vortex and of the suction-side branch of the horseshoe vortex along the suction surface. Furthermore, the transitional-flow computation also shows that the suction-side leg of the horseshoe vortex interacts with the separation bubble. This is a typical flow configuration for low-pressure turbine cascades in which high-loss fluid is fed into the separation bubble, whereas the rest is convected downstream with the vortex.

## Conclusions

A methodology for computing transitional flows through turbomachinery cascades is provided. The Reynolds-averaged Navier–Stokes equations for compressible flows are solved together with an EASM and $k$–$\omega$ turbulence closure. Furthermore, the model for separated-flow transition proposed by Mayle[1] has been employed. The governing equations are solved by an efficient numerical methodology, which is second-order accurate in space and time. First, the turbulence model has been validated computing the vortex shedding behind a two-dimensional turbine cascade. Then, the two-dimensional transitional flow through the T106 low-pressure turbine cascade has been computed to study the separated-flow transition that occurs at the suction side of the blade. Numerical results for the transition onset and the length of the separation bubble have been compared with experimental data for different values of the inlet turbulence intensity. The following conclusions can be drawn. 1) When the $k$–$\omega$ EASM without transition model was employed, the separation bubble could be predicted only for low inlet turbulence intensities ($Tu < 1\%$). 2) When the transition model of Mayle was employed, the bubble has been detected in all of the investigated range of the inlet turbulence intensity ($0.8\% < Tu < 7.1\%$), with the numerical results being in fairly good agreement with the experimental data. 3) Better agreement between the numerical and the experimental data is found for low–medium levels of $Tu$. Finally, the three-dimensional flow through the T106 linear turbine cascade has been computed, providing a description of the interaction between the secondary-flow pattern and the separation bubble. Note that an improved prediction of the loss-coefficient distribution has been achieved performing transitional-flow computations with respect to fully turbulent-flow computations.

## Acknowledgments

The author is grateful to M. Napolitano for his valuable suggestions and comments. Thanks are also due to L. Fottner, who kindly provided the experimental inlet flow data for the T106 cascade.

## References

[1]Mayle, R. E., "The Role of Laminar–Turbulent Transition in Gas Turbine Engines," *Journal of Turbomachinery*, Vol. 113, No. 4, 1991, pp. 509–537.

[2]Wilcox, D. C., *Turbulence Models for CFD*, DCW Industries, Inc., La Cañada, CA, 1998.

[3]De Palma, P., Pascazio, G., and Napolitano, M., "Accurate and Efficient Solutions of Unsteady Viscous Flows," *International Journal of Numerical Methods for Heat and Fluid Flow*, Vol. 11, No. 4, 2001, pp. 286–307.

[4]De Palma, P., "Numerical Simulation of Transitional Turbomachinery Flows," *Computational Fluid Dynamics 2000*, edited by N. Satofuka, Springer-Verlag, Berlin, 2001, pp. 449–454.

[5]Gatski, T. B., and Speziale, C. G., "On Explicit Algebraic Stress Models for Complex Turbulent Flows," *Journal of Fluid Mechanics*, Vol. 254, 1993, pp. 59–78.

[6]Cicatelli, G., and Sieverding, C. H., "The Effect of Vortex Shedding on the Unsteady Pressure Distribution Around the Trailing Edge of a Turbine Blade," *Journal of Turbomachinery*, Vol. 119, No. 4, 1997, pp. 810–819.

[7]Hoheisel, H., Kiock, R., Lichtfuss, H. J., and Fottner, L., "Influence of Free-Stream Turbulence and Blade Pressure Gradient on Boundary Layer and Loss Behavior of Turbine Cascades," *Journal of Turbomachinery*, Vol. 109, No. 4, 1987, pp. 210–219.

[8]Menter, F. R., and Rumsey, C. L., "Assessment of Two-Equation Turbulence Models for Transonic Flows," AIAA Paper 94-2343, 1994.

[9]Launder, B. E., Reece, G. J., and Rodi, W., "Progress in the Development of a Reynolds Stress Turbulence Closure," *Journal of Fluid Mechanics*, Vol. 68, 1975, pp. 537–566.

[10]Gatski, T., Abid, R., and Rumsey, C., "Prediction of Nonequilibrium Turbulent Flows with Explicit Algebraic Stress Models," *AIAA Journal*, Vol. 33, No. 11, 1995, pp. 2026–2031.

[11]Dhawhan, S., and Narasimha, R., "Some Properties of Boundary Layer Flow During Transition from Laminar to Turbulent Motion," *Journal of Fluid Mechanics*, Vol. 3, 1958, pp. 418–436.

[12]Roe, P. L., "Approximate Riemann Solvers, Parameter Vectors and Difference Schemes," *Journal of Computational Physics*, Vol. 43, No. 2, 1981, pp. 357–372.

[13]Arnone, A., Liou, M., and Povinelli, L. A., "Intergration of Navier–Stokes Equations Using Dual Time Stepping and a Multigrid Method," *AIAA Journal*, Vol. 33, No. 6, 1995, pp. 985–990.

[14]Martinelli, L., and Jameson, A., "Validation of a Multigrid Method for the Reynolds Averaged Equations," AIAA Paper 88-0414, 1988.

[15]Brandt, A., *Guide to Multigrid Development*, Lecture Notes in Mathematics, Vol. 960, Springer-Verlag, Berlin, 1982, pp. 220–312.

[16]Jameson, A., "Time-Dependent Calculations Using Multigrid, with Applications to Unsteady Flows Past Airfoils and Wings," AIAA Paper 91-1596, 1991.

[17]Manna, M., Mulas, M., and Cicatelli G., "Vortex Shedding Behind a Blunt Trailing Edge Blade," *International Journal of Turbo and Jet Engines*, Vol. 14, No. 3, 1997, pp. 145–157.

[18]Hildebrandt, T., and Fottner, L., "A Numerical Study of the Influence of Grid Refinement and Turbulence Modeling on the Flow Field Inside a Highly Loaded Turbine Cascade," *Journal of Turbomachinery*, Vol. 121, No. 4, 1999, pp. 709–716.

[19]Hoheisel, H., "Test Case E/CA-6 Subsonic Turbine Cascade T106," *Test Cases for Computation of Internal Flows in Aero Engine Components*, edited by L. Fottner, AR-275, AGARD, 1990, pp. 112–123.

R. M. C. So
*Associate Editor*